An isogeometric analysis approach to gradient damage models

Clemens V. Verhoosel[1,2,*,†], Michael A. Scott[2], Thomas J. R. Hughes[2]
and René de Borst[1]

[1]*Department of Mechanical Engineering, Eindhoven University of Technology,*
5600 MB Eindhoven, The Netherlands
[2]*Institute for Computational Engineering and Sciences, University of Texas at Austin, Austin, TX 78712, U.S.A.*

SUMMARY

Continuum damage formulations are commonly used for the simulation of diffuse fracture processes. Implicit gradient damage models are employed to avoid the spurious mesh dependencies associated with local continuum damage models. The C^0-continuity of traditional finite elements has hindered the study of higher order gradient damage approximations. In this contribution we use isogeometric finite elements, which allow for the construction of higher order continuous basis functions on complex domains. We study the suitability of isogeometric finite elements for the discretization of higher order gradient damage approximations. Copyright © 2011 John Wiley & Sons, Ltd.

1. INTRODUCTION

Continuum damage models [1] are widely used for the simulation of diffuse fracture processes. Several modifications of the original theory have been proposed to overcome the mesh dependency problems associated with the absence of an internal length scale (see e.g. [2, 3]). One way to avoid mesh dependencies is to relate the material parameters to the element size [4–6]. Alternatively, an internal length scale can be introduced by a spatial smoothing function in the continuum formulation [7]. Gradient approximations of this smoothing function have led to the development of damage models where an internal length scale is introduced through gradients of an equivalent strain field. Regularization can also be established by smoothening of e.g. the damage parameter, but we choose to regularize the formulation by means of the strain measure because of its implementational simplicity. Among the gradient damage formulations, the implicit gradient enhancement [8] is considered the most effective. In its original form a second-order Taylor expansion is used to approximate a smoothing integral, which results in a system of two second-order partial differential equations. This formulation is attractive from a discretization point of view since it can be solved using C^0-continuous finite elements. It has, however, been demonstrated that the accuracy of the second-order approximation can be limited [9, 10]. For that reason it is important to study the effect of the higher order terms in the Taylor approximation of the nonlocal formulation, which result in higher order gradient damage formulations.

---

*Correspondence to: Clemens V. Verhoosel, Department of Mechanical Engineering, Eindhoven University of Technology, 5600 MB Eindhoven, The Netherlands.
†E-mail: c.v.verhoosel@tue.nl

Mixed finite element formulations can be used for the discretization of higher order gradient (damage) formulations (see Reference [11] for an application in gradient-dependent plasticity). In these formulations, the introduction of higher order continuous basis functions is avoided by introducing auxiliary fields. This results in systems with many more degrees of freedom than required by the second-order gradient formulation, making the method computationally expensive. It is important to distinguish the auxiliary fields introduced in a mixed formulation from the equivalent strain field used in implicit gradient damage formulations. In the latter case, the additional field emanates from the model, and not from the discretization. To avoid the introduction of auxiliary fields, meshless methods have been used [10]. The smoothness of meshless methods is inherently derived from the way in which the basis functions are constructed. Although meshless methods have been applied successfully for the discretization of the fourth-order gradient damage formulation, they have not been used widely. A reason for this is that the study of the fourth-order model in Reference [12] has led to the conclusion that the gain in accuracy obtained from the higher order terms does not outweigh the increase in complexity resulting from the meshless method. The inability of meshless methods to define geometry [13] and the incompatibility with traditional finite element formulations, in the sense that the method is not element-based, may be other reasons why meshless methods are not commonly applied to higher order gradient damage formulations.

In this contribution we use isogeometric finite elements to overcome the problems associated with the use of mixed formulations and meshless methods for gradient damage formulations. The isogeometric analysis concept was introduced by Hughes *et al.* [14] and has been applied successfully to a wide variety of problems in solids, fluids and fluid–structure interactions (see [15] for an overview). Use of higher order, smooth spline bases in isogeometric analysis has computational advantages over standard finite elements, especially when higher order differential equations are considered [16]. In contrast to meshless methods, the geometry and solution space are fully coupled. This makes it possible to construct bases for complex geometries, which can be obtained directly from a computer-aided design (CAD) tool [17, 18]. From an analysis point of view isogeometric analysis can be considered as an element-based discretization technique [19, 20]. This compatibility with traditional finite elements facilitates the application to industrial problems.

We first review the nonlocal continuum damage formulation and the gradient-based approximation in Section 2. We then introduce in Section 3 the isogeometric finite element discretization and present an element-based representation for smooth spline bases. In Section 4 we present numerical simulations utilizing isogeometric finite elements for the discretization of the second-order, fourth-order and sixth-order gradient formulations.

2. ISOTROPIC DAMAGE FORMULATION

We consider a body $\Omega \subset \mathbb{R}^N$ with $N \in \{1, 2, 3\}$ and boundary $\partial\Omega$ (see Figure 1). The displacement of a material point $x \in \Omega$ is denoted by $u(x) \in \mathbb{R}^N$. The displacements satisfy Dirichlet boundary
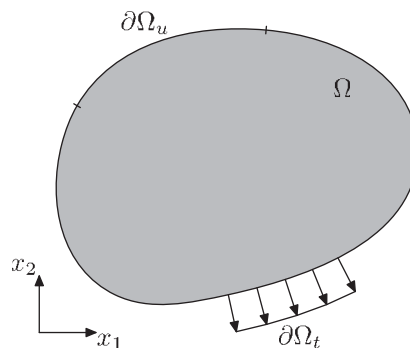

Figure 1. Solid domain Ω with boundary $\partial\Omega$.

conditions, $u_i = \tilde{u}_i$, on $\partial\Omega_{u_i} \subseteq \partial\Omega$. Under the assumption of small displacement gradients, the infinitesimal strain tensor

$$\varepsilon_{ij} = u_{(i,j)} = \frac{1}{2}\left(\frac{\partial u_i}{\partial x_j} + \frac{\partial u_j}{\partial x_i}\right) \tag{1}$$

is used as an appropriate measure for the deformation of the body. The Cauchy stress tensor, $\sigma(x) \in \mathbb{R}^{N \times N}$, is used as the corresponding stress measure. An external traction $\tilde{t}_i$ acts on the Neumann boundary $\partial\Omega_{t_i} \subseteq \partial\Omega$ and is equal to the projection of the stress tensor on the outward pointing normal vector $n(x) \in \mathbb{R}^N$, i.e. $t_i = \sigma_{ij}n_j$. The solid body is loaded by increasing the boundary tractions or boundary displacements. We refer to a stepwise increase in the boundary conditions as a load step.

2.1. Constitutive modeling

In isotropic continuum damage models, the Cauchy stress is related to the infinitesimal strain tensor by

$$\sigma_{ij} = (1-\omega)H_{ijkl}\varepsilon_{kl}, \tag{2}$$

where $\omega \in [0, 1]$ is a scalar damage parameter and H is the Hookean elasticity tensor for undamaged material (i.e. with $\omega = 0$). When damage has fully developed ($\omega = 1$) a material has lost all stiffness. Note that we adopt index notation with summation from 1 to N over repeated italic indices, for example, $u_i v_i = \sum_{i=1}^{N} u_i v_i$.

The damage parameter is related to a history parameter κ by a monotonically increasing function $\omega = \omega(\kappa)$, which is referred to as the damage law. Various damage laws will be considered in Section 4. The history parameter evolves according to the Kuhn–Tucker conditions

$$f \leqslant 0, \quad \dot{\kappa} \geqslant 0, \quad \dot{\kappa}f = 0 \tag{3}$$

for the loading function $f = \bar{\eta} - \kappa$, where $\bar{\eta}$ is a nonlocal strain measure, referred to as the nonlocal equivalent strain. The monotonicity of both κ and $\omega(\kappa)$ guarantees that the damage parameter is monotonically increasing at every material point, thereby introducing irreversibility in the constitutive model.

Nonlocality is introduced into the model by means of the nonlocal equivalent strain that ensures a well-posed formulation at the onset of damage evolution. If instead the damage parameter was related to a local strain measure, η, the resulting medium would suffer from a local loss of ellipticity in the case of material softening [21]. The model is then unable to smear out the damage zone over a finite volume. In other words, a local continuum damage formulation fails to introduce a length scale for the damage zone, resulting in spurious mesh dependencies in numerical solutions.

A straightforward way of introducing nonlocality in the formulation is by defining the nonlocal equivalent strain, $\bar{\eta}(x)$, as the volume average of the local equivalent strain, $\eta = \eta(\varepsilon)$

$$\bar{\eta}(x) = \frac{\int_{y \in \Omega} g(x, y)\eta(y)\,dy}{\int_{y \in \Omega} g(x, y)\,dy}, \tag{4}$$

where $g(x, y)$ is the weighting function

$$g(x, y) = \exp\left(-\frac{\|x-y\|^2}{2l_c^2}\right). \tag{5}$$

We refer to this model as the nonlocal damage formulation [7]. The local equivalent strain maps the strain tensor onto a scalar. In Section 4 we will employ various equivalent strain relations.

Although the nonlocal formulation is straightforward, it requires the computation of a volume integral for the evaluation of the constitutive behavior at every material point. This makes the numerical implementation both cumbersome and inefficient. In particular, the stiffness matrix is

full. Even when truncated, the nonlocal operator has a negative impact on the sparsity of the matrix. This results in computationally expensive assembly and solution routines. To circumvent these deficiencies, approximations of the integral equation are commonly used.

The nonlocal equivalent strain (4) can be approximated by substitution of a Taylor expansion for the equivalent strain field around the point x

$$\eta(y) = \eta|_{y=x} + \left.\frac{\partial \eta}{\partial y_i}\right|_{y=x}(y_i - x_i) + \frac{1}{2}\left.\frac{\partial \eta}{\partial y_i \partial y_j}\right|_{y=x}(y_i - x_i)(y_j - x_j) + \mathcal{O}((x_i - y_i)^3). \qquad (6)$$

The gradient approximation of Equation (4) may be obtained by assuming the solid volume extends to infinity

$$\bar{\eta}(x) = \eta(x) + \frac{1}{2}l_c^2\frac{\partial^2 \eta}{\partial x_i^2}(x) + \frac{1}{8}l_c^4\frac{\partial^4 \eta}{\partial x_i^2 \partial x_j^2}(x) + \frac{1}{48}l_c^6\frac{\partial^6 \eta}{\partial x_i^2 \partial x_j^2 \partial x_k^2}(x) + \cdots. \qquad (7)$$

This gradient approximation is known as the explicit gradient formulation. As an alternative, the implicit gradient formulation (e.g. Reference [8]) is obtained by direct manipulation of Equation (7)

$$\bar{\eta}(x) - \frac{1}{2}l_c^2\frac{\partial^2 \bar{\eta}}{\partial x_i^2}(x) + \frac{1}{8}l_c^4\frac{\partial^4 \bar{\eta}}{\partial x_i^2 \partial x_j^2}(x) - \frac{1}{48}l_c^6\frac{\partial^6 \bar{\eta}}{\partial x_i^2 \partial x_j^2 \partial x_k^2}(x) + \cdots = \eta(x). \qquad (8)$$

The second-order implicit gradient formulation has enjoyed widespread use since for that case only C^0-continuity is required [8].

In the remainder of this work we study the convergence of the implicit gradient formulation toward the nonlocal formulation upon increasing the number of gradient terms involved. If we truncate Equation (8) after the dth derivative, we can rewrite it using a linear operator $\mathcal{L}^d$ as

$$\mathcal{L}^d\bar{\eta}(x) = \eta(x). \qquad (9)$$

We restrict ourselves to the second-order ($d=2$), fourth-order ($d=4$) and sixth-order ($d=6$) implicit gradient damage formulations.

2.2. Implicit gradient damage formulation

In contrast to the nonlocal and explicit gradient damage formulations, the implicit formulation requires the solution of a boundary value problem for the nonlocal equivalent strain field, $\bar{\eta}(x)$, in addition to the usual problem for the displacement field, $u(x)$. In the absence of body forces, the resulting boundary value problem for the dth-order formulation is given by

$$\begin{aligned}
\frac{\partial \sigma_{ij}}{\partial x_j} &= 0 \quad \forall x \in \Omega, \\
\mathcal{L}^d\bar{\eta} &= \eta, \\
\sigma_{ij}n_j &= \tilde{t}_i \quad \forall x \in \partial\Omega_{t_i}, \\
\frac{\partial}{\partial x_n}\left(\frac{\partial^\alpha \bar{\eta}}{\partial x_j \dots}\right) &= 0 \quad \forall x \in \partial\Omega, \, \alpha \in \{0, \dots, d-2\}, \\
u_i &= \tilde{u}_i \quad \forall x \in \partial\Omega_{u_i},
\end{aligned} \qquad (10)$$

where $\tilde{t}$ and $\tilde{u}$ are the prescribed boundary traction and displacements, respectively. Notice that we assume all directional derivatives, $\partial/\partial x_n = n_i(\partial/\partial x_i)$, of the nonlocal equivalent strain field zero on the boundary. We verify this choice numerically by comparing the results with the nonlocal formulation based on the integral equation (4). The kinematic and constitutive relations (1) and (2) are used to express the Cauchy stress in terms of the displacement field.

We solve the system (10) using the Galerkin method. The same solution spaces are used for the displacement field and nonlocal equivalent strain field, denoted by $\mathcal{S}_i^u \subset H^{\frac{d}{2}}(\Omega)$ and $\mathcal{S}^{\bar{\eta}} \subset H^{\frac{d}{2}}(\Omega)$,

respectively. This choice is consistent with the conclusions in Reference [22], where it is shown that the objective results can be obtained using the same order of interpolation for both fields. Thereby it is important to remark that the gradient damage formulations are coupled problems, rather than mixed formulations. As a consequence, the Babuška–Brezzi conditions do not apply. As a side-effect of using the same order of interpolation functions, stress oscillations have been observed [22]. In Section 4 we illustrate that higher order splines are less susceptible to these oscillations than linear basis functions.

We denote our trial spaces as $\mathscr{V}_i^u$ and $\mathscr{V}^{\bar{\eta}}$ and assume that $\mathscr{V}^{\bar{\eta}} = \mathscr{S}^{\bar{\eta}}$ and $\mathscr{V}_i^u$ and $\mathscr{S}_i^u$ are the same modulo inhomogeneous boundary conditions. The weak form of Equation (10) then follows as

$$(\sigma_{ij}, v_{(i,j)}^u)_\Omega = (\tilde{t}_i, v_i^u)_{\partial\Omega} \quad \forall v_i^u \in \mathscr{V}_i^u,$$

$$(\bar{\eta} - \eta, v^{\bar{\eta}})_\Omega + \sum_{\alpha=1}^{d/2} (\mathscr{H}^\alpha \bar{\eta}, \mathscr{H}^\alpha v^{\bar{\eta}})_\Omega = 0 \quad \forall v^{\bar{\eta}} \in \mathscr{V}^{\bar{\eta}},$$

(11)

where $v_{(i,j)}^u = \frac{1}{2}((\partial v_i^u / \partial x_j) + (\partial v_j^u / \partial x_i))$ and $(\cdot, \cdot)_\Omega$ is the L^2-inner product. We note that for our specific choice of the trial spaces, a trial function can be interpreted as a virtual displacement $v_i^u = \delta u_i$. In that case $v_{(i,j)}^u$ coincides with the virtual strain field $\delta\varepsilon_{ij}$ according to Equation (1). No boundary terms appear in the equation for the equivalent strain field, since the derivatives of this field in the direction of the normal vector are assumed zero on the boundary of the domain. For the damage formulations considered in this work (i.e. with $d \in \{2, 4, 6\}$), the linear operator $\mathscr{H}^\alpha$ is written as

$$\mathscr{H}^1 = \frac{l_c}{\sqrt{2}} \frac{\partial}{\partial x_i}, \quad \mathscr{H}^2 = \frac{l_c^2}{\sqrt{8}} \frac{\partial^2}{\partial x_i \partial x_j}, \quad \mathscr{H}^3 = \frac{l_c^3}{\sqrt{48}} \frac{\partial^3}{\partial x_i \partial x_j \partial x_k}.$$

(12)

For the sixth-order formulation it follows that

$$\sum_{\alpha=1}^{d/2} (\mathscr{H}^\alpha \bar{\eta}, \mathscr{H}^\alpha v^{\bar{\eta}})_\Omega = \int_\Omega \frac{l_c^2}{2} \frac{\partial\bar{\eta}}{\partial x_i} \frac{\partial v^{\bar{\eta}}}{\partial x_i} + \frac{l_c^4}{8} \frac{\partial^2\bar{\eta}}{\partial x_i \partial x_j} \frac{\partial^2 v^{\bar{\eta}}}{\partial x_i \partial x_j} + \frac{l_c^6}{48} \frac{\partial^3\bar{\eta}}{\partial x_i \partial x_j \partial x_k} \frac{\partial^3 v^{\bar{\eta}}}{\partial x_i \partial x_j \partial x_k} \, \mathrm{d}\Omega,$$

(13)

from which the fourth- and second-order results can be extracted by subsequently ignoring the third- and second-order spatial derivatives.

3. ISOGEOMETRIC FINITE ELEMENTS

Discretization of the weak formulation (11) for the dth-order damage formulation requires $((d/2) - 1)$-times continuously differentiable basis functions. With isogeometric finite elements C^{p-1}-continuous basis functions can be constructed using non-uniform rational B-splines (NURBS) [23] or T-splines [24] of order p. This means that suitable analysis bases can be constructed for the fourth- and sixth-order formulation by considering the basis functions of orders 2 and 3, respectively.

In this section we follow the developments in [19, 20] where the Bézier mesh, defined through an extraction operation, becomes our isogeometric finite element discretization. An automatic extraction operation exists for any NURBS or T-spline basis. This implies that all such spaces can be dealt with in a uniform way. Since many of these technologies are already in place, higher order continuous Bézier meshes can be created for many problems of engineering interest.

3.1. Univariate B-splines and NURBS

The fundamental building block of isogeometric analysis is the univariate B-spline, e.g. [15, 23]. A univariate B-spline is a piecewise polynomial defined over a knot vector $\Xi = \{\xi_1, \xi_2, \ldots, \xi_{n+p+1}\}$, with n and p denoting the number and order of basis functions, respectively. The knot values ξ_i

are non-decreasing with increasing knot index i, i.e. $\xi_1 \leqslant \xi_2 \leqslant \cdots \leqslant \xi_{n+p+1}$. We refer to the positive knot intervals as elements. B-splines used for analysis purposes are generally open B-splines. Since these are interpolatory at their boundary, the Dirichlet boundary conditions can be applied in a straightforward manner.

A B-spline of order p is defined as a linear combination of n B-spline basis functions

$$a(\xi) = \sum_{i=1}^{n} N_{i,p}(\xi) A_i, \tag{14}$$

where $N_{i,p}(\xi)$ represents a B-spline basis function of order p and A_i is called a control point or variable. Equation (14) is typically used for the parameterization of curves in two (with $A_i \in \mathbb{R}^2$) or three (with $A_i \in \mathbb{R}^3$) dimensions.

The B-spline basis is defined recursively, starting with the zeroth-order ($p=0$) functions

$$N_{i,0}(\xi) = \begin{cases} 1 & \xi_i \leqslant \xi < \xi_{i+1} \\ 0 & \text{otherwise} \end{cases} \tag{15}$$

from which the higher order ($p=1, 2, \ldots$) basis functions can be constructed using the Cox–de Boor recursion formula [25, 26]

$$N_{i,p}(\xi) = \frac{\xi - \xi_i}{\xi_{i+p} - \xi_i} N_{i,p-1}(\xi) + \frac{\xi_{i+p+1} - \xi}{\xi_{i+p+1} - \xi_{i+1}} N_{i+1,p-1}(\xi). \tag{16}$$

Efficient and robust algorithms exist for the evaluation of these non-negative basis functions and their derivatives, e.g. [27]. An example of a univariate B-spline basis is shown in Figure 2. B-spline basis functions satisfy the partition of unity property, and B-spline parameterizations possess the variation diminishing property, e.g. [28]. B-splines can also be refined, which is important in the context of isogeometric analysis, e.g. [29]. However, a drawback of B-splines is their inability to exactly represent many objects of engineering interest, such as conic sections. For this reason NURBS, which are a rational generalization of B-splines, are commonly used. A NURBS is defined as

$$a(\xi) = \sum_{i=1}^{n} R_{i,p}(\xi) A_i \tag{17}$$

with the NURBS basis functions defined as

$$R_{\alpha,p}(\xi) = \frac{N_{\alpha,p}(\xi) W_\alpha}{w(\xi)}, \tag{18}$$

where $w(\xi) = \sum_{i=1}^{n} N_{i,p}(\xi) W_i$ is called the weighting function. Note that in Equation (18) no summation is performed over the repeated greek index α. In the special case that $W_i = c \ \forall i \in \{1, \ldots, n\}$, and c an arbitrary constant, the NURBS basis reduces to the B-spline basis. For notational convenience, we will drop the subscript p of the B-spline and NURBS basis functions.
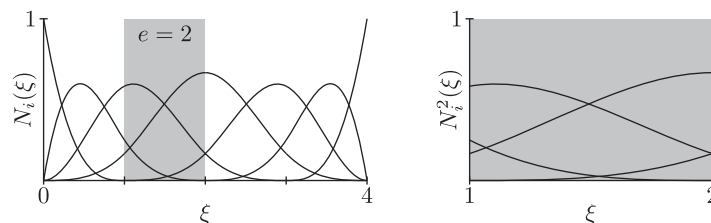

Figure 2. Third-order B-spline basis for the global knot vector $\Xi = \{0, 0, 0, 0, 1, 2, 3, 4, 4, 4, 4\}$ (left) and the restrictions of the nonzero basis functions $\{N_i^e\}$ to element 2 ($e=2$) (right).
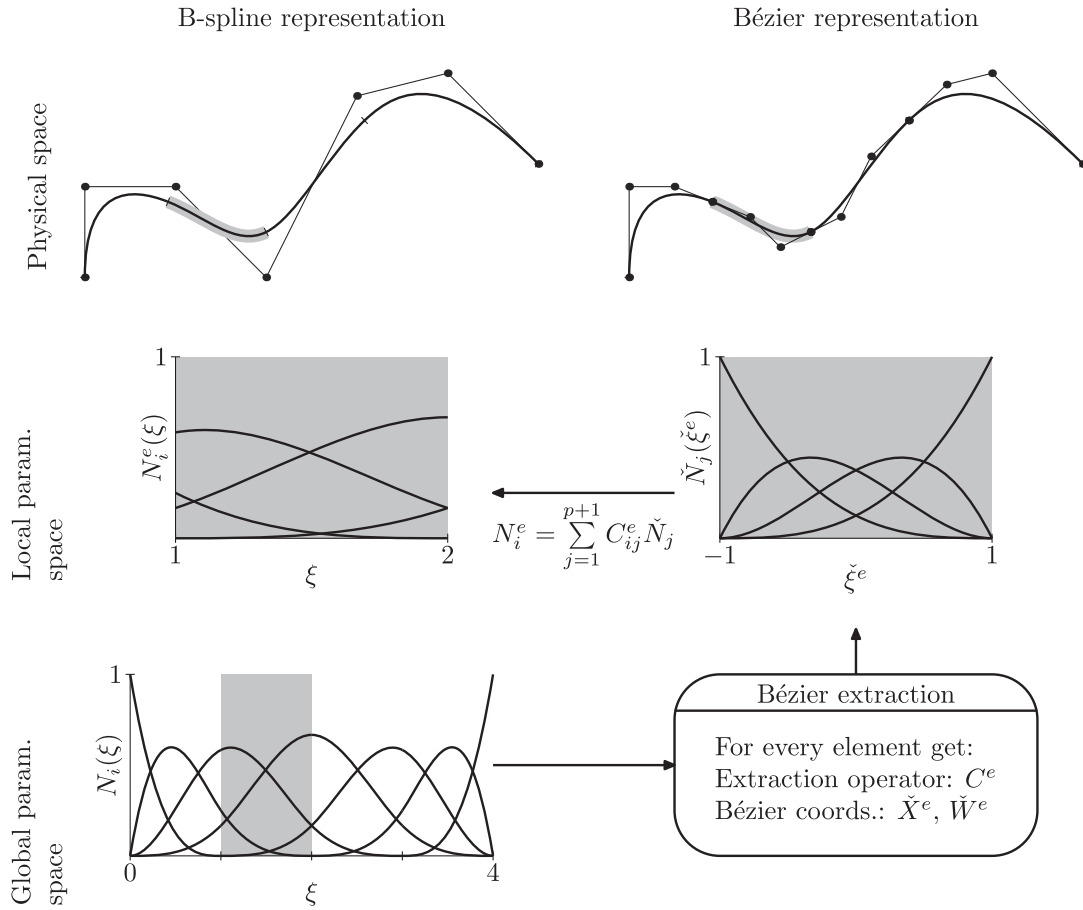
B-spline representation   Bézier representation

Figure 3. Schematic representation of the Bézier extraction process.

$$N_i^e = \sum_{j=1}^{p+1} C_{ij}^e \check{N}_j$$

Bézier extraction

For every element get:
Extraction operator: C^e
Bézier coords.: $\check{X}^e$, $\check{W}^e$

3.2. The Bézier mesh

A univariate NURBS basis is suitable for the analysis of the higher order gradient damage formulations in the sense that the continuity requirements can be met by selecting the correct order of the polynomials. The notion of an element, as being a knot interval of positive length, is useful from a numerical point of view, since it allows for piecewise evaluation of the integrals (11) using quadrature rules. The NURBS basis functions are not local to the elements, that is, for every element e the basis functions, $\{N_i^e\}$, are different (see Figure 2).

For higher order B-spline bases a canonical basis can be extracted using Bézier extraction. We illustrate the concept of Bézier extraction for the univariate case (see Figure 3). The B-spline basis shown in Figure 2 can be used to create a two-dimensional curve as shown in Figure 3. Such a curve is composed of several elements $[\xi_{k(e)}, \xi_{k(e)+1})$, each with its own set of restricted basis functions $\{N_i^e(\xi)\}$. Now let us define the affine map

$$\check{\xi}^e(\xi) = \frac{2\xi - \xi_{k(e)} - \xi_{k(e)+1}}{\xi_{k(e)+1} - \xi_{k(e)}}, \tag{19}$$

which by definition ranges from -1 to 1. We refer to this local knot span as the univariate Bézier element. We can now construct a B-spline basis which is local to this Bézier element $[-1, 1)$. This basis, known as the Bernstein basis, is shown in the right column of Figure 3. Since both the restricted B-spline basis $\{N_i^e\}$ and the Bernstein basis $\{\check{N}_j\}$ span the space of polynomials of

order p restricted to the element e, we can write

$$N_i^e(\xi) = \sum_{j=1}^{p+1} C_{ij}^e \check{N}_j(\check{\xi}^e(\xi)), \tag{20}$$

where the matrix C^e is the extraction operator [19, 20]. This extraction operator can be efficiently obtained by means of knot insertion in the global B-spline basis. The process of obtaining the extraction operators for every element is referred to as Bézier extraction, see [19, 20] for details of the extraction process.

From Figure 3 it is observed that the B-spline basis for every element can be constructed in two different, but equivalent, ways: (i) by restricting the global basis functions to the element; (ii) by mapping the Bézier element basis functions onto the B-spline element using the extraction operator. We prefer the representation of the basis by Bézier elements and extraction operators because it generalizes to the multivariate non-tensor product T-spline setting.

Bézier extraction allows for the construction of a Bézier mesh, over which a higher order continuous spline basis can be constructed. An analysis suitable Bézier mesh consists of:

- A collection of Bézier elements, each of which is provided with the same set of basis functions $\{\check{N}_j\}$ and a different extraction operator C^e for each element.
- A global set of control point positions, $X \in \mathbb{R}^{n \times N}$, and weights, $W \in \mathbb{R}^n$, from which the Bézier positions and weights can easily be obtained using $\check{X}_i^e = C_{ji}^e X_j$ and $\check{W}_i^e = C_{ji}^e W_j$.

Since a multivariate Bézier element can be defined as a tensor product of the univariate element, as illustrated in Figure 4 for the bivariate case, the Bézier mesh provides a uniform treatment of any global spline basis for which extraction operators can be defined. The extraction process has been studied in detail for univariate and multivariate NURBS [19, 20]. Extraction operators can also be derived for multivariate T-spline meshes. Since Bézier extraction operators can be constructed for T-splines, higher order continuous Bézier meshes can be created for a large variety of geometries of engineering interest.
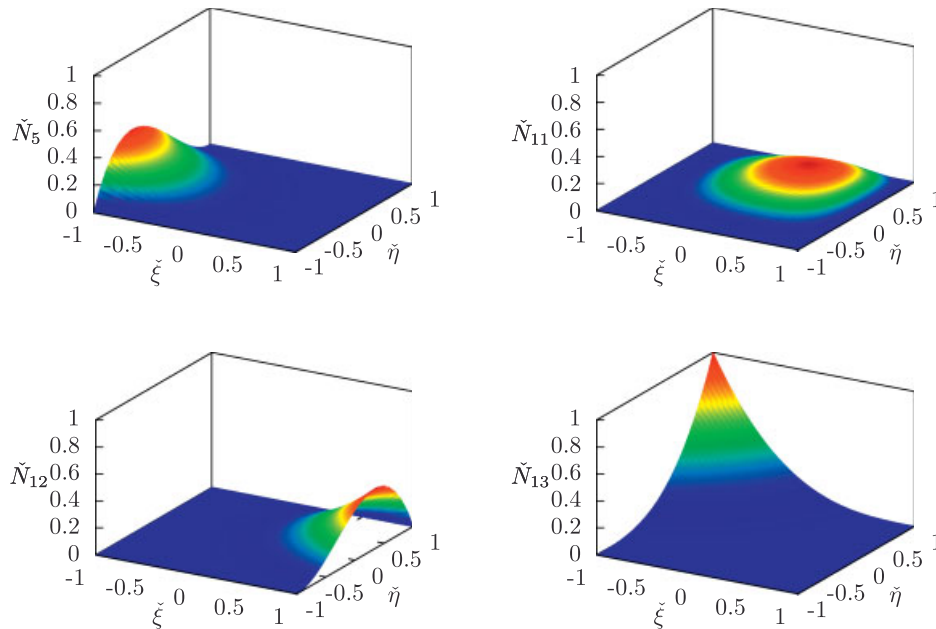

Figure 4. Some basis functions for the bicubic Bézier element. The bivariate basis functions are defined as the tensor product of two univariate cubic Bézier elements, $\check{N}_a(\check{\xi}, \check{\eta}) = \check{N}_i(\check{\xi})\check{N}_j(\check{\eta})$, with $a = (p+1)(j-1)+i$.

The Bézier extraction operators C^e map the Bézier element basis functions onto a B-spline basis. In the case that a global NURBS basis is required, the B-spline basis functions are transformed into NURBS basis functions by Equation (17). Since we consider Bézier meshes for which the global control point positions and weights are provided, this transformation can be evaluated.

3.3. Isogeometric finite element discretization

Let $\mathscr{S}_i^{u,h} \subset \mathscr{S}_i^u$ and $\mathscr{S}^{\bar{\eta},h} \subset \mathscr{S}^{\bar{\eta}}$ be the discrete solution spaces for the displacement field, $u(x)$, and nonlocal equivalent strain field, $\bar{\eta}(x)$, respectively. These spaces are written in terms of the basis functions defined over the Bézier mesh, $\{R_i(x)\}$. We can approximate the displacement field and nonlocal equivalent strain field as

$$u_i^h(x) = \sum_{k=1}^n R_k(\xi(x))U_{ki},$$
$$\bar{\eta}^h(x) = \sum_{k=1}^n R_k(\xi(x))H_k, \tag{21}$$

where $U \in \mathbb{R}^{n \times N}$ are the control point displacements, and $H \in \mathbb{R}^n$ the control point nonlocal equivalent strains. From the displacement field, the strain, $\varepsilon(x)$, and local equivalent strain, $\eta(x)$, can be computed. In combination with the nonlocal equivalent strain field, the damage parameter, $\omega(x)$, and Cauchy stress, $\sigma(x)$, can be obtained at every point using the constitutive relations provided in Section 2.1.

We use the Galerkin method to discretize the weak formulation (11) as

$$(\sigma_{ij}, v_{(i,j)}^{u,h})_\Omega = (\tilde{t}_i, v_i^{u,h})_{\partial\Omega} \quad \forall v_i^{u,h} \in \mathscr{V}_i^{u,h},$$
$$(\bar{\eta} - \eta, v^{\bar{\eta},h})_\Omega + \sum_{\alpha=1}^{d/2} (\mathscr{H}^\alpha \bar{\eta}, \mathscr{H}^\alpha v^{\bar{\eta},h})_\Omega = 0 \quad \forall v^{\bar{\eta},h} \in \mathscr{V}^{\bar{\eta},h}. \tag{22}$$

Using the NURBS basis functions, $\{R_i(x)\}$, as trial functions results in a system of $(N+1)n$ equations

$$f_{\text{int},k}^{u_m} = f_{\text{ext},k}^{u_m} \quad \forall (k,m) \in \{1 \dots n\} \otimes \{1 \dots N\},$$
$$f_{\text{int},k}^{\bar{\eta}} = 0 \qquad \forall k \in \{1 \dots n\}, \tag{23}$$

which can be solved for every load step using Newton–Raphson iteration to determine the control point coefficients U_{ki} and H_k in Equation (21). The internal force vectors are assembled by looping over the Bézier elements

$$f_{\text{int},k}^{u_m} = \overset{n_e}{\underset{e=1}{\mathbf{A}}} f_{\text{int},k}^{e,u_m} = \overset{n_e}{\underset{e=1}{\mathbf{A}}} \left(\sigma_{ij}, \frac{1}{2} \left(\frac{\partial R_k^e}{\partial x_j} \delta_{im} + \frac{\partial R_k^e}{\partial x_i} \delta_{jm} \right) \right)_{\Omega_e},$$
$$f_{\text{int},k}^{\bar{\eta}} = \overset{n_e}{\underset{e=1}{\mathbf{A}}} f_{\text{int},k}^{e,\bar{\eta}} = \overset{n_e}{\underset{e=1}{\mathbf{A}}} (\bar{\eta} - \eta, R_k^e)_{\Omega_e} + \sum_{\alpha=1}^{d/2} (\mathscr{H}^\alpha \bar{\eta}, \mathscr{H}^\alpha R_k^e)_{\Omega_e}, \tag{24}$$

where the element internal force vectors can be expressed in terms of the Bézier basis functions by substitution of

$$R_\alpha^e(\xi) = \frac{W_\alpha \sum_{j=1}^{(p+1)^N} C_{\alpha j}^e \check{N}_j(\check{\xi}^e(\xi))}{\sum_{i=1}^n W_i \sum_{j=1}^{(p+1)^N} C_{ij}^e \check{N}_j(\check{\xi}^e(\xi))} = \frac{W_\alpha \sum_{j=1}^{(p+1)^N} C_{\alpha j}^e \check{N}_j(\check{\xi}^e(\xi))}{\sum_{j=1}^{(p+1)^N} \check{W}_j^e \check{N}_j(\check{\xi}^e(\xi))}. \tag{25}$$

Hence, the internal force vectors can be assembled using the Bézier mesh. The integrals in Equation (24) are evaluated on the Bézier elements. In this contribution, we use Gaussian quadrature of order $p+1$ in each direction. Accordingly, increasing the polynomial order p will increase

the number of integration points per elements. While keeping the number of elements the same, this will lead to a significant increase in computational effort (in particular of the assembly operations). However, at least for the numerical simulations considered in this paper, the required number of elements to obtain a specified accuracy decreases with increasing polynomial order, see Section 4.1. As a consequence, the computational burden of increasing the smoothness of the basis is limited for these cases. Numerical integration of NURBS for analysis purposes was studied in [30] and remains an active topic of research.

In order to evaluate the integrals over the Bézier elements, the Jacobian of the isogeometric map needs to be evaluated at every integration point. Since rational basis functions are used, this requires application of the quotient rule. Since higher order derivatives with respect to the physical coordinate x are used in this contribution, higher order derivatives of the parametric map are also required (see Appendix A).

The consistent tangent matrix, required by the Newton–Raphson procedure, can be obtained by differentiation of (24) with respect to the control point variables in Equation (21) to get

$$K_{ks}^{u_m u_t} = \overset{n_e}{\underset{e=1}{\mathbf{A}}} K_{ks}^{e,u_m u_t}, \quad K_{ks}^{u_m \bar{\eta}} = \overset{n_e}{\underset{e=1}{\mathbf{A}}} K_{ks}^{e,u_m \bar{\eta}}, \quad K_{ks}^{\bar{\eta} u_t} = \overset{n_e}{\underset{e=1}{\mathbf{A}}} K_{ks}^{e,\bar{\eta} u_t}, \quad K_{ks}^{\bar{\eta}\bar{\eta}} = \overset{n_e}{\underset{e=1}{\mathbf{A}}} K_{ks}^{e,\bar{\eta}\bar{\eta}} \tag{26}$$

with

$$
\begin{aligned}
K_{ks}^{e,u_m u_t} &= \left(\frac{1}{2} \left(\frac{\partial R_s^e}{\partial x_r} \delta_{qt} + \frac{\partial R_s^e}{\partial x_q} \delta_{rt} \right) \frac{\partial \sigma_{ij}}{\partial \varepsilon_{qr}}, \frac{1}{2} \left(\frac{\partial R_k^e}{\partial x_j} \delta_{im} + \frac{\partial R_k^e}{\partial x_i} \delta_{jm} \right) \right)_{\Omega_e}, \\
K_{ks}^{e,u_m \bar{\eta}} &= \left(R_s^e \frac{\partial \sigma_{ij}}{\partial \bar{\eta}}, \frac{1}{2} \left(\frac{\partial R_k^e}{\partial x_j} \delta_{im} + \frac{\partial R_k^e}{\partial x_i} \delta_{jm} \right) \right)_{\Omega_e}, \\
K_{ks}^{e,\bar{\eta} u_t} &= - \left(\frac{1}{2} \left(\frac{\partial R_s^e}{\partial x_r} \delta_{qt} + \frac{\partial R_s^e}{\partial x_q} \delta_{rt} \right) \frac{\partial \eta}{\partial \varepsilon_{qr}}, R_k^e \right)_{\Omega_e}, \\
K_{ks}^{e,\bar{\eta}\bar{\eta}} &= (R_s^e, R_k^e)_{\Omega_e} + \sum_{\alpha=1}^{d/2} (\mathscr{H}^\alpha R_s^e, \mathscr{H}^\alpha R_k^e)_{\Omega_e}.
\end{aligned}
\tag{27}
$$

Upon substitution of Equation (25) these element stiffness matrices can be evaluated for every Bézier element. The derivatives of the stress, σ, with respect to the strain, ε, and nonlocal equivalent strain, $\bar{\eta}$, are provided through the constitutive behavior elaborated in Section 2.1. The derivative of the local equivalent strain, η, with respect to the strain tensor follows from the equivalent strain law, $\eta = \eta(\varepsilon)$.

4. NUMERICAL SIMULATIONS

4.1. One-dimensional rod loaded in tension

We consider a one-dimensional rod loaded in tension as shown in Figure 5. The central section of the rod has a reduced cross-sectional area in order to develop a centralized damage zone. The modulus of elasticity of the rod is $E = 20\,\text{GPa}$, and the Cauchy stress is written as $\sigma = (1 - \omega)E\varepsilon$.
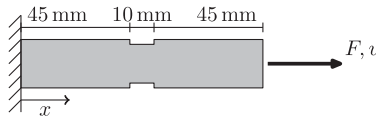

Figure 5. Schematic representation of a one-dimensional rod loaded in tension. The cross-sectional area of the rod is $10\,\text{mm}^2$ except for the central section where it is equal to $9\,\text{mm}^2$.
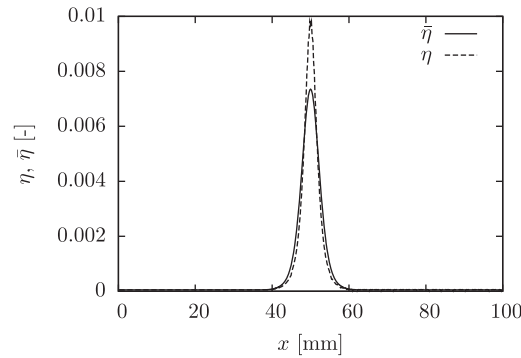
Figure 6. Comparison of the local equivalent strain field η and the nonlocal equivalent strain field $\bar{\eta}$ at $u = 0.048$. The result is obtained using the sixth-order formulation and 1280 cubic Bézier elements.

Table I. Meshes used for the uniaxial rod simulation.

Linear Bézier elements ($p=1$)					
Number of elements (n_e)	80	160	320	640	1280
Number of basis functions (n)	81	161	321	641	1281
Cubic Bézier elements ($p=3$)					
Number of elements (n_e)	80	160	320	640	1280
Number of basis functions (n)	83	163	323	643	1283

As a damage law, we consider [8]

$$\omega(\kappa) = \begin{cases} 0 & \kappa \leqslant \kappa_0 \\ \dfrac{\kappa_u}{\kappa} \dfrac{\kappa - \kappa_0}{\kappa_u - \kappa_0} & \kappa > \kappa_0 \end{cases} \tag{28}$$

with $\kappa_0 = 1 \times 10^{-4}$ and $\kappa_u = 0.0125$. We define the local equivalent strain law as $\eta = \langle \varepsilon \rangle$, where $\langle \cdot \rangle$ is the Macaulay bracket and take the nonlocal length scale in (5) equal to $l_c = \sqrt{2}$ mm. The smoothening effect of this nonlocal length scale on the equivalent strain field is illustrated in Figure 6.

Force–displacement curves have been determined for the nonlocal damage formulation, and for the second-, fourth- and sixth-order implicit gradient models. A dissipation-based path-following constraint [31] is used to trace the equilibrium path beyond the snapback point. Mesh convergence studies have been performed using uniform meshes with 80, 160, 320, 640 and 1280 linear and cubic Bézier elements (with all control weights equal to 1). An overview of the meshes is given in Table I. Note that in contrast to higher order finite elements, the number of degrees of freedom is practically independent of the order of the basis.

In Figure 7, we show the force–displacement curves for all formulations obtained on cubic Bézier meshes. The force F acting on the right end of the rod is plotted versus the displacement of the point to which it is applied, see Figure 5. For the second-order formulation a minor variation in the force–displacement curves is observed when increasing the number of elements from 640 to 1280. For the higher order formulations and the nonlocal formulation, the response obtained on the 1280 element mesh cannot be visually distinguished from that obtained on the 640 element mesh. This improved convergence behavior is attributed to the fact that the higher order formulations and nonlocal formulation generate smoother results than the second-order formulation. The increased smoothness of the higher order formulations and the nonlocal formulation is closely related to the postponed loss of ellipticity for these formulations as demonstrated by the dispersion analysis performed in [10]. For the purpose of comparing the various formulations, the accuracy of the solutions obtained on the 1280 element meshes suffices. In Figure 8, we show the force–displacement curves for the
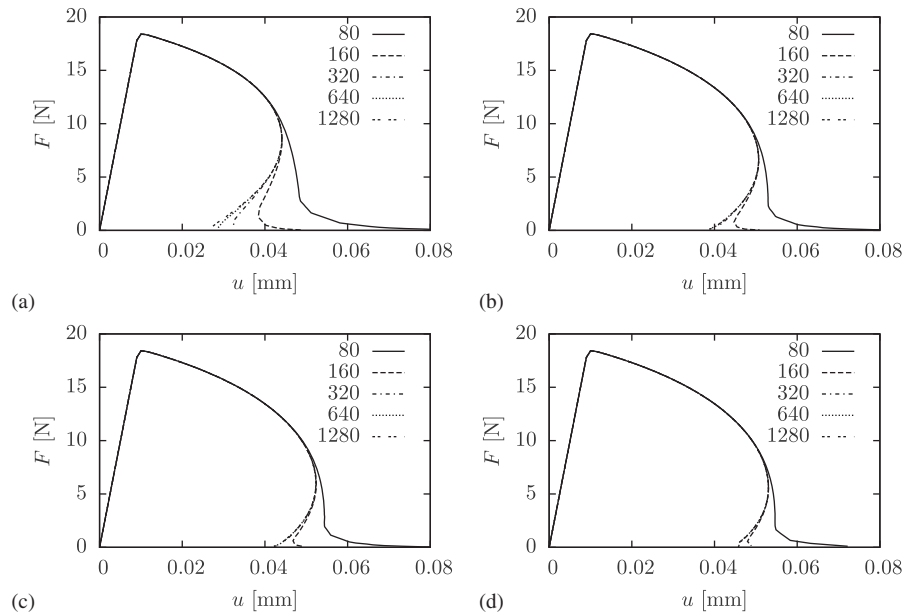
Figure 7. Mesh convergence studies for the rod using cubic B-splines for the second-order (a), fourth-order (b) and sixth-order (c) gradient damage formulations, and for the nonlocal formulation (d). The key labels indicate the number of Bézier elements.
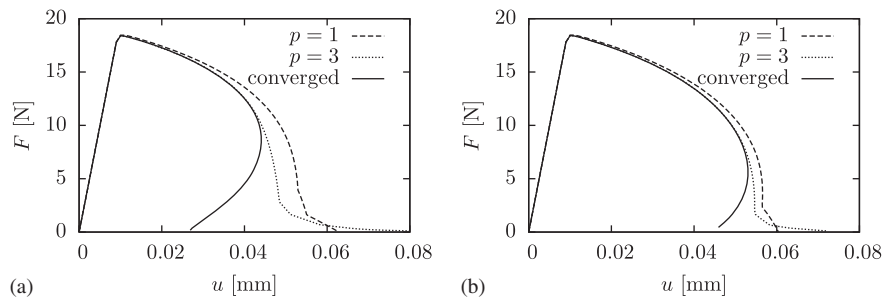

Figure 8. Comparison of the results obtained with 80 Bézier elements of order one ($p=1$) and order three ($p=3$) for the second-order gradient (a) and nonlocal (b) damage formulation.

second-order gradient formulation and nonlocal formulation obtained using 80 Bézier elements of order one and order three. Meaningful results for the higher order formulations cannot be obtained using linear elements. Comparison of the results for linear B-splines with the results obtained using cubic B-splines shows the superior convergence behavior of cubic basis functions. A detailed study of the convergence rates is a topic of future research. In Figure 9, we show the Cauchy stress in the rod as a function of the position. For linear basis functions we observe the same oscillatory behavior as in Reference [22]. When we use higher order continuous basis functions for the second-order formulation, the oscillations are observed to be reduced drastically. For the sixth-order formulation, for which only third-order splines are used, the observed stress oscillations are also very limited.

In Figure 10, we show a comparison of the various formulations. All results are obtained on a cubic Bézier mesh with 1280 elements. The results are in excellent agreement with those reported in e.g. [8, 10]. As in [10] it is observed that the incorporation of fourth-order derivatives in the implicit scheme improves the results, in the sense that the obtained force–displacement curve is closer to that of the nonlocal formulation. Consistent with this observation we find that the sixth-order formulation gives an even better approximation of the nonlocal result. Similar trends are observed from the final damage profiles (see Figure 11). The sixth-order formulation is found to be very
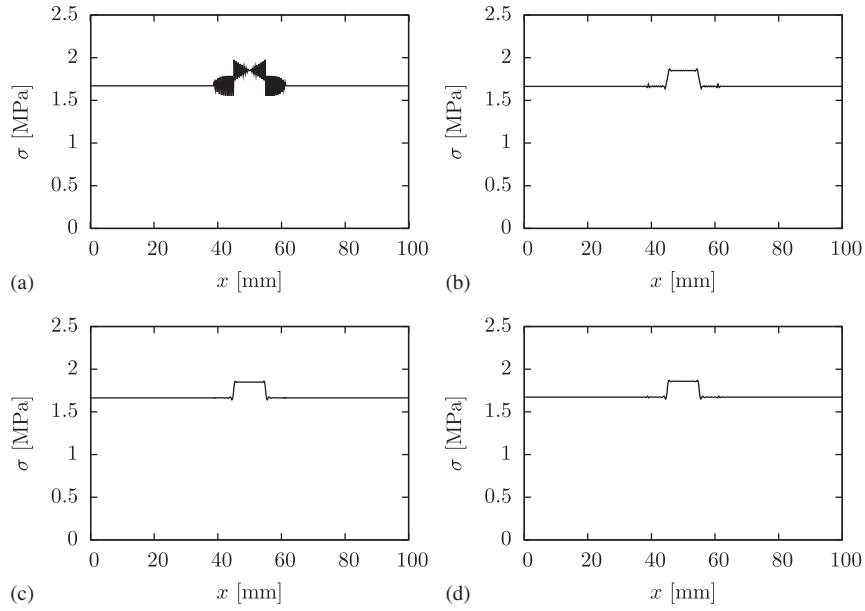
Figure 9. Cauchy stress in the one-dimensional rod at $u = 0.023$ mm for the second-order gradient damage formulation with linear basis functions (a), quadratic basis functions (b), and cubic basis functions (c), and for the sixth-order formulation with cubic basis functions (d). The stress is plotted in the integration points.
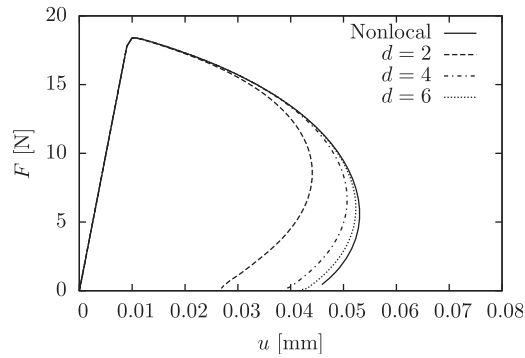

Figure 10. Force–displacement diagrams for the rod loaded in tension using the nonlocal formulation and dth-order gradient formulations. All results are obtained using cubic Bézier meshes with 1280 elements.
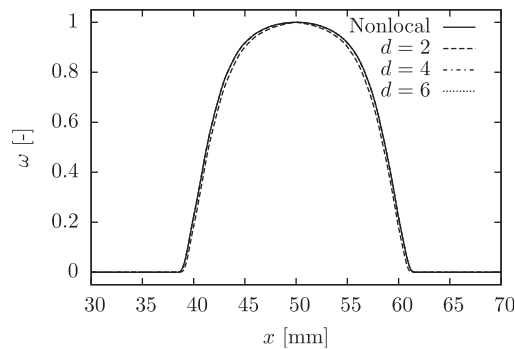
Figure 11. Final damage profile for the rod loaded in tension using the nonlocal formulation and the dth-order gradient formulations. All results are obtained using cubic Bézier meshes with 1280 elements.
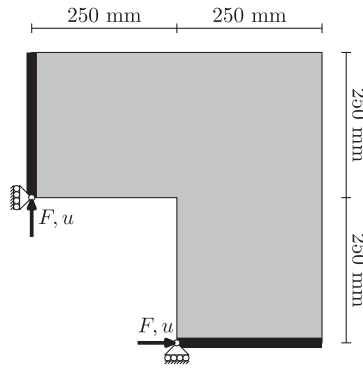
Figure 12. L-shaped specimen. The thickness of the specimen is 200 mm.

efficient since the results are in good agreement with the nonlocal formulation, while the involved computational effort is very small compared to the nonlocal formulation. Based on the resemblance of the sixth-order and nonlocal result it is concluded that, for the considered simulation, ignoring the nonlocal equivalent strain boundary terms appearing in the gradient formulation has a minor effect on the results.

4.2. L-shaped specimen

As a second numerical experiment, we consider the L-shaped specimen shown in Figure 12. The problem set-up is inspired by Kuhl [32], but has been modified to illustrate the capabilities of isogeometric finite elements. The free rotation of the rigid end-plates is incorporated by means of linear constraints on the boundary control points, which is possible due to the fact that the basis functions on the corresponding boundaries can exactly represent all affine motions and in particular rigid rotations and translations. The diagonal failure zone resulting from the set-up requires mesh refinements in that direction, which can be achieved using analysis-suitable T-splines.

In the undamaged state a linear isotropic material is considered with the modulus of elasticity $E = 10$ GPa and Poisson's ratio $v = 0.2$. Plane stress conditions are assumed. The modified Von Mises local equivalent strain proposed in [2] is used

$$\eta(\varepsilon) = \frac{k-1}{2k(1-2v)} I_1(\varepsilon) + \frac{1}{2k} \sqrt{\left(\frac{k-1}{1-2v} I_1(\varepsilon)\right)^2 + \frac{12k}{(1+v)^2} J_2(\varepsilon)}, \tag{29}$$

where $I_1(\varepsilon) = \varepsilon_{ii}$ and $J_2(\varepsilon) = \frac{1}{2}\varepsilon'_{ij}\varepsilon'_{ij}$ are the first invariant of the strain tensor and second invariant of the deviatoric strain tensor, $\varepsilon'_{ij} = \varepsilon_{ij} - \frac{1}{3}\varepsilon_{kk}\delta_{ij}$, respectively. Note that in the plane stress case, the summations in the expressions for the strain invariants are taken from 1 to 3. The parameter $k = 10$ distinguishes the cases of tension and compression, as illustrated in Figure 13. The following damage law proposed in [33] is used

$$\omega(\kappa) = \begin{cases} 0 & \kappa \leqslant \kappa_0 \\ 1 - \dfrac{\kappa_0}{\kappa}\{(1-\alpha) + \alpha \exp[\beta(\kappa_0 - \kappa)]\} & \kappa > \kappa_0 \end{cases} \tag{30}$$

with parameters $\kappa_0 = 4 \times 10^{-4}$, $\alpha = 0.98$ and $\beta = 80$. The nonlocal length scale is taken as $l_c = 5\sqrt{2} \approx 7.07$ mm.

Force–displacement curves are obtained using the cubic Bézier meshes as shown in Figure 14. A summary of the mesh parameters is given in Table II. Note that for the third-order T-spline
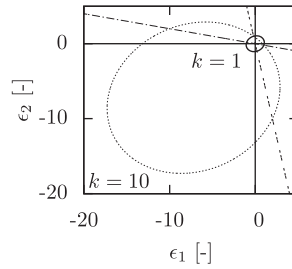
Figure 13. Modified Von Mises equivalent strain definition for $k=1$ and $k=10$. The isolines for $\eta=1$ are shown in the principal strain space under the conditions of plane stress. The dashed lines represent the cases of uniaxial loading.
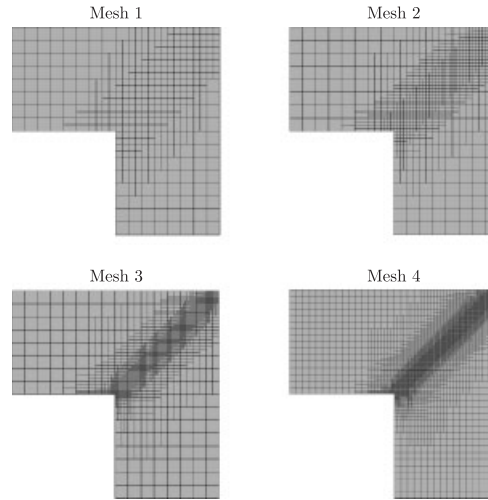

Figure 14. Bézier meshes for the L-shaped specimen.

Table II. Bézier meshes used for the L-shaped specimen.

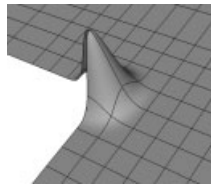|	Mesh 1	Mesh 2	Mesh 3	Mesh 4
Spline order (p)	3	3	3	3
Number of elements (n_e)	391	816	1686	6032
Number of basis functions (n)	473	832	1543	5714

Figure 15. Smooth (C^2) basis function centered around the reentrant corner of the L-shaped domain.

the number of basis functions is similar to the number of elements, this in contrast to traditional cubic finite elements. A C^2-continuous base mesh is created using a non-tensor product T-spline. The C^2 basis function centered around the reentrant corner is shown in Figure 15. Meshes 1, 2 and 3 are obtained by the subsequent local refinements of a band along the symmetry plane. Mesh 4
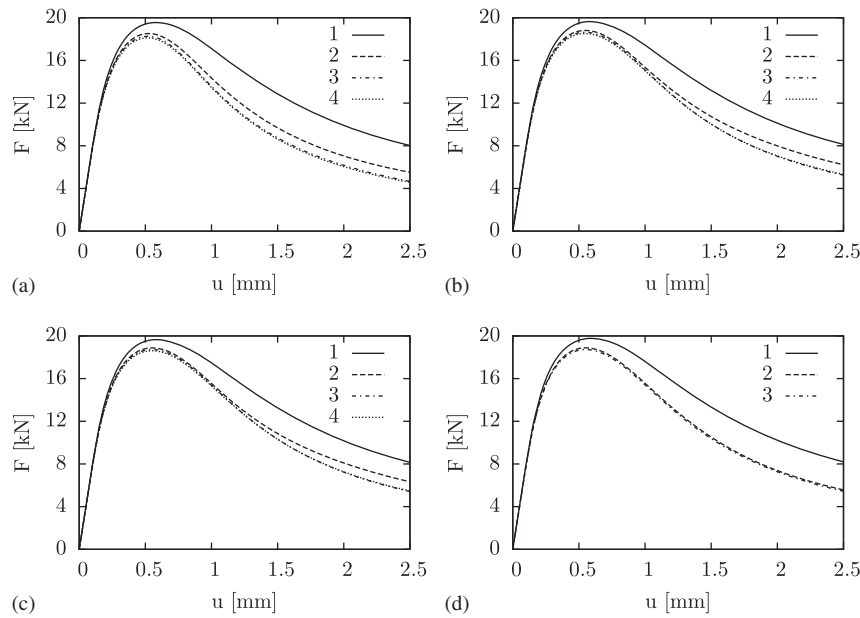
Figure 16. Mesh convergence studies using the cubic T-spline meshes in Figure 14 for the second-order
(a), fourth-order (b) and sixth-order (c) damage formulations, and for the nonlocal formulation (d).
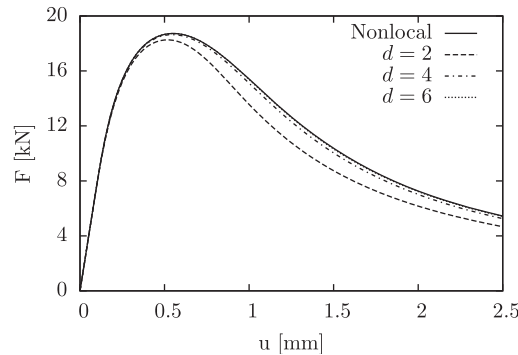

Figure 17. Force–displacement results for the L-shaped specimen using the nonlocal formulation and
*d*th-order gradient formulations. All results are obtained using Mesh 3.

is obtained as a global refinement of Mesh 3. The control point weights are all taken equal to 1.
Displacement control is used to trace the equilibrium path.

The force–displacement curves obtained using the various meshes are shown in Figure 16.
The force F and displacement u are defined in Figure 12. For the gradient formulations, the
results obtained on Mesh 3 cannot be visually distinguished from those obtained using Mesh 4.
As observed for the uniaxial rod, better convergence behavior is obtained by increasing the order
of the formulation. Because of the involved computational effort, the force–displacement curves
for the nonlocal formulation are obtained only on Meshes 1, 2 and 3. The force–displacement
curve obtained on Mesh 3 coincides with that found on Mesh 2. For all formulations, the accu-
racy of the result obtained on Mesh 3 is sufficient to allow for comparison of the various
formulations.

In Figure 17, the results of the various formulations are compared. Upon increasing the order
of the formulation the approximation of the nonlocal result is improved. Increasing the order of
the formulation increases the total amount of dissipated energy. This is caused by the additional
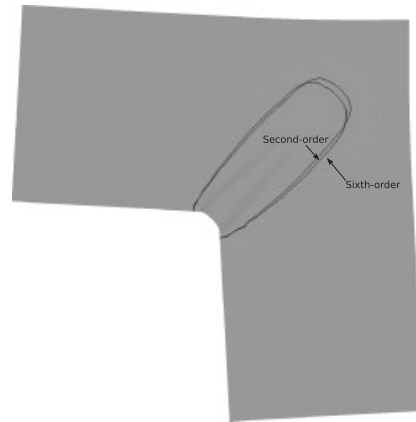
Figure 18. Isolines for the damage parameter $\omega = 0.8$ in the L-shaped specimen at $u = 2\,mm$ as computed on Mesh 3 by the second-order formulation and the sixth-order formulation. Displacements are amplified by a factor of 15.
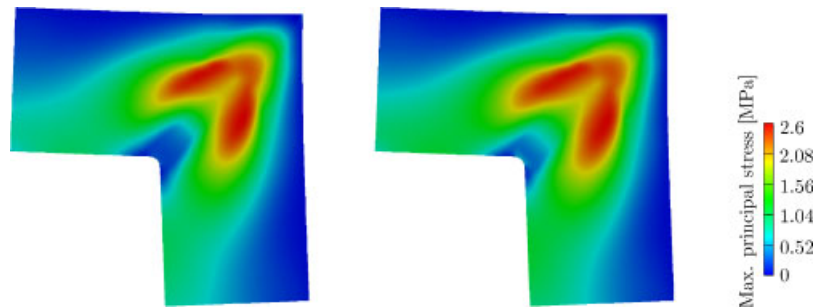

Figure 19. Maximum principal stress contours at $u = 1.25\,mm$ as computed on Mesh 3 by the second-order (left) formulation and the sixth-order formulation (right). Displacements are amplified by a factor of 15.

smoothing effect of the higher order derivatives, which can also be seen from the damage isolines in Figure 18. In Figure 19, we show the maximum principal stress contours for the second-order and sixth-order formulations. No substantial stress oscillations are observed from these figures, which is consistent with the observations for the one-dimensional simulation in Figure 9(c) and (d). For the considered problem, the sixth-order formulation is observed to be very efficient, since it accurately approximates the nonlocal result, whereas the involved computational effort is negligible compared with the nonlocal formulation. As in the case of the rod simulation, setting all the Neumann boundary conditions (10) for the equivalent strain field to zero does not have a significant effect on the results.

5. CONCLUSIONS

Isogeometric analysis allows for the construction of smooth basis functions on complex domains, providing an appropriate solution space for higher order differential equations. The Dirichlet boundary conditions can be applied by specifying control variables along the boundary, in the same way as nodal variables are specified for traditional finite elements. The higher order basis functions can be constructed on an element level by means of Bézier extraction, which provides compatibility with traditional finite element implementations.

Isogeometric analysis is shown to be a very good candidate for the discretization of higher order gradient damage formulations. Using cubic basis functions allows for the discretization of

the sixth-order gradient damage formulation. In contrast to traditional finite elements, the number of degrees of freedom is practically independent of the polynomial order of the basis functions. Although the required number of integration points per element increases upon increasing the polynomial order, the improved convergence rate generally allows for the use of coarser meshes. For the considered simulations, the fourth- and sixth-order formulations require only slightly more computational effort than the second-order formulation. This makes it practical to study the convergence of the implicit gradient damage formulation toward the nonlocal formulation upon increasing its order.

Numerical simulations have been performed for a one-dimensional rod loaded in tension, for which a univariate B-spline basis is constructed. A two-dimensional L-shaped specimen is discretized using Bézier elements, for which the extraction operators have been determined using an underlying T-spline. For both simulations it is observed that the result of the nonlocal formulation is approached upon increasing the order of the gradient damage formulation. Since the computational effort involved in the nonlocal formulation is much larger than that for the gradient approximations, increasing the order of the gradient formulation yields efficient approximations of the nonlocal result. For the two simulations considered, the sixth-order formulation turned out to give an accurate approximation.

A more detailed study of the mesh convergence behavior of isogeometric finite elements is a topic of further study. In the gradient damage formulations, the approximation behavior, and in particular its dependence on the smoothing length, also needs to be studied in more detail.

APPENDIX A: BASIS FUNCTION DERIVATIVES

For the assembly of the internal force vector and corresponding tangent, discussed in Section 3, the derivatives of the basis function with respect to the physical coordinates are required. In the two-dimensional case, we can compute the first-order derivatives by the differentiation of

$$R(\xi, \eta) = \tilde{R}(x(\xi, \eta), y(\xi, \eta)) \tag{A1}$$

to yield the system

$$\begin{pmatrix} R_\xi \\ R_\eta \end{pmatrix} = \begin{bmatrix} x_\xi & y_\xi \\ x_\eta & y_\eta \end{bmatrix} \begin{pmatrix} \tilde{R}_x \\ \tilde{R}_y \end{pmatrix}, \tag{A2}$$

where the subscripts are used to indicate differentiation. Since efficient and robust algorithms exist for the computation of the derivatives with respect to the parametric coordinates, e.g. [27], the basis function derivatives with respect to the physical coordinates are obtained by

$$\begin{pmatrix} \tilde{R}_x \\ \tilde{R}_y \end{pmatrix} = \frac{1}{x_\xi y_\eta - x_\eta y_\xi} \begin{bmatrix} y_\eta & -y_\xi \\ -x_\eta & x_\xi \end{bmatrix} \begin{pmatrix} R_\xi \\ R_\eta \end{pmatrix}. \tag{A3}$$

Using these results, the second-order basis function derivatives with respect to the physical coordinate are obtained by solving the system

$$\begin{bmatrix} x_\xi^2 & 2x_\xi y_\xi & y_\xi^2 \\ x_\xi x_\eta & x_\xi y_\eta + x_\eta y_\xi & y_\xi y_\eta \\ x_\eta^2 & 2x_\eta y_\eta & y_\eta^2 \end{bmatrix} \begin{pmatrix} \tilde{R}_{xx} \\ \tilde{R}_{xy} \\ \tilde{R}_{yy} \end{pmatrix} = \begin{pmatrix} R_{\xi\xi} \\ R_{\xi\eta} \\ R_{\eta\eta} \end{pmatrix} - \begin{bmatrix} x_{\xi\xi} & y_{\xi\xi} \\ x_{\xi\eta} & y_{\xi\eta} \\ x_{\eta\eta} & y_{\eta\eta} \end{bmatrix} \begin{pmatrix} \tilde{R}_x \\ \tilde{R}_y \end{pmatrix} \tag{A4}$$

and subsequently, the third-order derivatives are obtained as

$$
\begin{bmatrix}
x_\xi^3 & 3x_\xi^2 y_\xi & 3x_\xi y_\xi^2 & y_\xi^3 \\
x_\xi^2 x_\eta & x_\xi^2 y_\eta + 2x_\xi x_\eta y_\xi & x_\eta y_\xi^2 + 2x_\xi y_\xi y_\eta & y_\xi^2 y_\eta \\
x_\xi x_\eta^2 & x_\eta^2 y_\xi + 2x_\xi x_\eta y_\eta & x_\xi y_\eta^2 + 2x_\eta y_\xi y_\eta & y_\xi y_\eta^2 \\
x_\eta^3 & 3x_\eta^2 y_\eta & 3x_\eta y_\eta^2 & y_\eta^3
\end{bmatrix}
\begin{pmatrix}
\tilde{R}_{xxx} \\
\tilde{R}_{xxy} \\
\tilde{R}_{xyy} \\
\tilde{R}_{yyy}
\end{pmatrix}
$$

$$
= \begin{pmatrix}
R_{\xi\xi\xi} \\
R_{\xi\xi\eta} \\
R_{\xi\eta\eta} \\
R_{\eta\eta\eta}
\end{pmatrix}
- \begin{bmatrix}
3x_\xi x_{\xi\xi} & 3x_\xi y_{\xi\xi} + 3x_{\xi\xi} y_\xi & 3y_\xi y_{\xi\xi} \\
2x_\xi x_{\xi\eta} + x_\eta x_{\xi\xi} & 2x_\eta y_\xi + 2x_\xi y_{\xi\eta} + x_{\xi\xi} y_\eta + x_\eta y_{\xi\xi} & 2y_\xi y_{\xi\eta} + y_\eta y_{\xi\xi} \\
2x_\eta x_{\xi\eta} + x_\xi x_{\eta\eta} & 2x_\eta y_\eta + 2x_\eta y_{\xi\eta} + x_{\eta\eta} y_\xi + x_\xi y_{\eta\eta} & 2y_\eta y_{\xi\eta} + y_\xi y_{\eta\eta} \\
3x_\eta x_{\eta\eta} & 3x_\eta y_{\eta\eta} + 3x_{\eta\eta} y_\eta & 3y_\eta y_{\eta\eta}
\end{bmatrix}
\begin{pmatrix}
\tilde{R}_{xx} \\
\tilde{R}_{xy} \\
\tilde{R}_{yy}
\end{pmatrix}
$$

$$
- \begin{bmatrix}
x_{\xi\xi\xi} & y_{\xi\xi\xi} \\
x_{\xi\xi\eta} & y_{\xi\xi\eta} \\
x_{\xi\eta\eta} & y_{\xi\eta\eta} \\
x_{\eta\eta\eta} & y_{\eta\eta\eta}
\end{bmatrix}
\begin{pmatrix}
\tilde{R}_x \\
\tilde{R}_y
\end{pmatrix}. \tag{A5}
$$

Similar results can be obtained in the three-dimensional case.

REFERENCES

1. Lemaitre J, Chaboche JL. *Mechanics of Solid Materials*. Cambridge University Press: Cambridge, 1990.
2. de Vree JHP, Brekelmans WAM, van Gils MAJ. Comparison of nonlocal approaches in continuum damage mechanics. *Computers and Structures* 1995; **55**(4):581–588.
3. de Borst R. Damage, material instabilities, and failure. *Encyclopedia of Computational Mechanics*, *Vol. 2*: *Solids and Structures* (Chapter 10). Wiley: Chichester, 2004; 335–373.
4. Bazant ZP, Oh BH. Crack band theory for fracture of concrete. *Materials and Structures* 1983; **16**(3):155–177.
5. Willam KJ, Bicanic N, Stura S. Constitutive and computational aspects of strain-softening and localization in solids. *Constitutive Equations*: *Macro and Computational Aspects*. ASME: New York, 1984; 233.
6. Brekelmans WAM, de Vree JHP. Reduction of mesh sensitivity in continuum damage mechanics. *Acta Mechanica* 1995; **110**(1):49–56.
7. Pijaudier-Cabot G, Bažant ZP. Nonlocal damage theory. *Journal of Engineering Mechanics* 1987; **113**(10): 1512–1533.
8. Peerlings RHJ, de Borst R, Brekelmans WAM, de Vree JHP. Gradient enhanced damage for quasi-brittle materials. *International Journal for Numerical Methods in Engineering* 1996; **39**(19):3391–3403.
9. Huerta A, Pijaudier-Cabot G. Discretization influence on regularization by two localization limiters. *Journal of Engineering Mechanics* 1994; **120**(6):1198–1218.
10. Askes H, Pamin J, de Borst R. Dispersion analysis and element-free Galerkin solutions of second- and fourth-order gradient-enhanced damage models. *International Journal for Numerical Methods in Engineering* 2000; **49**(6):811–832.
11. De Borst R, Pamin J. Some novel developments in finite element procedures for gradient-dependent plasticity. *International Journal for Numerical Methods in Engineering* 1996; **39**(14):2477–2505.
12. Askes H, Sluys LJ. Explicit and implicit gradient series in damage mechanics. *European Journal of Mechanics— A/Solids* 2002; **21**(3):379–390.
13. Sakurai H. Element-free methods vs mesh-less CAE. *International Journal of Computational Methods* 2006; **3**(4):445–464.
14. Hughes T, Cottrell J, Bazilevs Y. Isogeometric analysis: CAD, finite elements, NURBS, exact geometry and mesh refinement. *Computer Methods in Applied Mechanics and Engineering* 2005; **194**(39–41):4135–4195.

15. Cottrell JA, Hughes TJR, Bazilevs Y. *Isogeometric Analysis*: *Toward Integration of CAD and FEA*. Wiley: Chichester, 2009.
16. Gómez H, Calo VM, Bazilevs Y, Hughes TJR. Isogeometric analysis of the Cahn-Hilliard phase-field model. *Computer Methods in Applied Mechanics and Engineering* 2008; **197**(49–50):4333–4352.
17. Cottrell JA, Reali A, Bazilevs Y, Hughes TJR. Isogeometric analysis of structural vibrations. *Computer Methods in Applied Mechanics and Engineering* 2006; **195**(41–43):5257–5296.
18. Benson DJ, Bazilevs Y, De Luycker E, Hsu MC, Scott M, Hughes TJR, Belytschko T. A generalized finite element formulation for arbitrary basis functions: from isogeometric analysis to xfem. *International Journal for Numerical Methods in Engineering* 2010; **83**(6):765–785.
19. Borden MJ, Scott MA, Evans JA, Hughes TJR. Isogeometric finite element data structures based on Bézier extraction. *International Journal for Numerical Methods in Engineering* 2010; DOI: 10.1002/nme.2968.
20. Scott MA, Borden MJ, Verhoosel CV, Sederberg TW, Hughes TJR. Isogeometric finite element data structures based on Bézier extraction of T-splines. *International Journal for Numerical Methods in Engineering*, submitted.
21. Sluys LJ, de Borst R. Dispersive properties of gradient-dependent and rate-dependent media. *Mechanics of Materials* 1994; **18**(2):131–149.
22. Simone A, Askes H, Peerlings RHJ, Sluys LJ. Interpolation requirements for implicit gradient-enhanced continuum damage models. *Communications in Numerical Methods in Engineering* 2003; **19**(7):563–572.
23. Rogers DF. *An Introduction to NURBS*. Academic Press: San Diego, 2001.
24. Sederberg TW, Zheng J, Bakenov A, Nasri A. T-splines and T-NURCCs. *ACM Transactions on Graphics* 2003; **22**(3):477–484.
25. Cox MG. The numerical evaluation of B-splines. *IMA Journal of Applied Mathematics* 1972; **10**(2):134–149.
26. de Boor C. On calculating with B-splines. *Journal of Approximation Theory* 1972; **6**(1):50–62.
27. Piegl L, Tiller W. *The NURBS Book*. Springer: Berlin, 1997.
28. Farin G. *Curves and Surfaces for CAGD*. Academic Press, Inc.: New York, 1993.
29. Cottrell JA, Hughes TJR, Reali A. Studies of refinement and continuity in isogeometric structural analysis. *Computer Methods in Applied Mechanics and Engineering* 2007; **196**(41–44):4160–4183.
30. Hughes TJR, Reali A, Sangalli G. Efficient quadrature for NURBS-based isogeometric analysis. *Computer Methods in Applied Mechanics and Engineering* 2010; **199**(5-8):301–313.
31. Verhoosel CV, Remmers JJC, Gutiérrez MA. A dissipation-based arc-length method for robust simulation of brittle and ductile failure. *International Journal for Numerical Methods in Engineering* 2009; **77**(9):1290–1321.
32. Kuhl E. Numerical models for cohesive frictional materials. *Ph.D. Thesis*, University of Stuttgart, 2000.
33. Geers MGD, de Borst R, Brekelmans WAM, Peerlings RHJ. Strain-based transient-gradient damage model for failure analyses. *Computer Methods in Applied Mechanics and Engineering* 1998; **160**(1–2):133–153.